

A Fixed-Grid Affine-Constrained Multiwavelet Coefficient Method for Buckley–Leverett Shock Capturing

Christian Tantardini^{1,*} and Evgueni Dinvai^{2,†}

¹*Center for Integrative Petroleum Research, King Fahd University of Petroleum and Minerals, Dhahran 31261, Saudi Arabia.*

²*Hylleraas Center, Department of Chemistry, UiT The Arctic University of Norway,
PO Box 6050 Langnes, N-9037 Tromsø, Norway*

(Dated: May 21, 2026)

We present a fixed-grid conservative affine-constrained modal/multiwavelet coefficient method for one-dimensional Buckley–Leverett saturation transport. The saturation is evolved directly in a local orthonormal coefficient basis with a mean/detail structure: the first mode carries the conservative cell average, whereas higher modes carry zero-mean local details. The hyperbolic inflow condition is imposed as a linear trace constraint on the coefficient vector and enforced by affine lifting. For $p > 1$, the boundary reprojection is applied in the detail subspace of the inflow cell, so that the prescribed trace is restored without modifying the conservative cell-average update. The transport operator is discretized in conservative weak form with monotone numerical fluxes, and shock-induced oscillations are controlled by a troubled-cell limiter acting on modal details.

The method is validated on a Berea-core waterflood benchmark against an independent `pywaterflood` reference solution using the same Corey fractional-flow closure, physical parameters, and pore-volume-injected scaling. The affine-constrained coefficient solver reproduces the reference breakthrough curve and saturation profiles, preserves the imposed inflow trace to roundoff accuracy, controls saturation bounds through mean-preserving detail rescaling, and gives small accumulated global mass-balance defects. Mesh-refinement, flux-comparison, and modal-order studies show that $p = 2$, corresponding to a piecewise-linear local representation, provides the most favorable accuracy–cost compromise among the tested orders for this shock-dominated benchmark.

I. INTRODUCTION

Accurate prediction of immiscible two-phase displacement is central to reservoir engineering, because decisions on well placement, injection strategy, breakthrough control, and sweep efficiency depend on reliable saturation-front dynamics in porous media [1–3]. At the continuum level, these processes are commonly described by incompressible two-phase flow, combining Darcy’s law, phase mass conservation, and a Buckley–Leverett-type saturation equation [4–6]. In the purely convective limit, the saturation equation is hyperbolic and may generate entropy shocks and rarefactions even from smooth initial data [7]. When capillary or dynamic-capillary effects are retained, the same transport structure is regularized by parabolic or pseudo-parabolic terms [8–10].

This distinction has direct numerical consequences. In the one-dimensional hyperbolic case with positive velocity, only the inflow boundary is prescribed, whereas the outflow trace is determined by the interior solution. By contrast, capillarity-regularized variants require additional boundary information. A coefficient-space discretization must therefore distinguish the physical imposition of boundary data from auxiliary analytical or numerical devices used to construct operators. This point is especially important for wavelet, multiwavelet, and modal formulations, where basis coefficients, traces, projections, and reconstructed fields do not automatically

satisfy pointwise boundary constraints unless the admissible coefficient space is explicitly enforced.

High-resolution saturation solvers are traditionally based on finite-volume methods, WENO-type reconstructions, discontinuous Galerkin schemes, and adaptive multiresolution strategies [11–14]. Wavelet and multiwavelet techniques have also been used for adaptivity, compression, stochastic representations, and uncertainty quantification [15–17]. In adaptive multiresolution schemes for conservation laws, the solution is represented on nested grid hierarchies, and detail or prediction coefficients are used to activate, discard, or refine resolution levels [18–20]. Recent multiresolution discontinuous Galerkin approaches similarly use hierarchical or multiwavelet representations to encode information across mesh levels and guide adaptive refinement [21, 22].

The present work develops a fixed-grid conservative coefficient-space solver for Buckley–Leverett shock propagation. The saturation is represented by cell-local orthonormal polynomial modes organized as a mean/detail hierarchy: the first mode carries the conservative cell average, whereas the higher modes carry zero-mean local detail information. This hierarchy is used as part of the numerical formulation itself. The inflow boundary condition is imposed as an affine constraint on the coefficients, oscillatory detail content is limited near shocks, and the mean coefficients retain a finite-volume-like conservative flux balance. All computations in this work are performed on fixed uniform partitions; no dynamic mesh refinement, coefficient thresholding, or sparse adaptive operator representation is used.

Although the weak residual is closely related to modal

* christiantantardini@gmail.com

† evgueni.dinvay@gmail.com

discontinuous Galerkin discretizations, the formulation is organized around coefficient-space operations rather than around reconstruction alone. The conservative mean mode enters the telescoping flux balance, the zero-mean detail modes provide the subcell degrees of freedom that are limited near shocks, and the inflow trace is handled as a linear functional of the coefficient vector. This organization keeps the boundary condition, limiter, and conservative update in the same set of unknowns.

The main contribution is the affine treatment of the hyperbolic inflow condition. The prescribed trace is written as a linear functional of the local coefficient vector and imposed as an affine constraint on the admissible coefficient space. For $p > 1$, where p is the number of local modes per cell, the stage reprojection is applied in the detail subspace of the inflow cell. This restores the imposed boundary trace without changing the mean coefficient of the inflow cell and therefore without modifying the conservative cell-average update.

The second ingredient is a conservative weak-form discretization of the Buckley–Leverett flux. Neighboring cells are coupled by monotone numerical interface fluxes, so that internal fluxes cancel pairwise in the global mass balance. The third ingredient is a troubled-cell limiter acting on zero-mean detail coefficients. The limiter suppresses nonphysical subcell oscillations near Buckley–Leverett shocks while preserving the cell averages that carry the conservative flux-difference update. The resulting method combines a finite-volume-like conservation structure with a fixed-grid modal/multiwavelet coefficient representation.

The method is validated on a Berea-core waterflood benchmark. The affine-constrained coefficient solver is compared with an independent `pywaterflood` reference calculation using the same Corey fractional-flow closure, physical parameters, and pore-volume-injected scaling [23]. The comparison includes breakthrough behavior, saturation profiles, flux sensitivity, mesh-refinement behavior, modal-order sensitivity, trace preservation, mass-balance diagnostics, and runtime.

The paper is organized as follows. Section II derives the Buckley–Leverett transport model and its one-dimensional hyperbolic reduction. Section III introduces the fixed-grid affine-constrained modal/multiwavelet coefficient formulation, including the weak residual, numerical fluxes, coefficient-space boundary constraint, limiter, and time integration. Section IV presents the Berea-core validation against the `pywaterflood` reference solution. Section V summarizes the results and outlines extensions.

II. BUCKLEY–LEVERETT MODEL

A. Two-phase flow equations

We consider immiscible, incompressible two-phase flow of a wetting phase w and a non-wetting phase o in a rigid porous medium. The porosity is $\phi(\mathbf{x})$, the absolute permeability tensor is $\mathbf{K}(\mathbf{x})$, and the phase saturations satisfy

$$S_w = S, \quad S_o = 1 - S. \quad (1)$$

The phase densities ρ_ℓ and viscosities μ_ℓ , with $\ell \in \{w, o\}$, are constant. The phase pressures are p_w and p_o , and the capillary pressure is defined by

$$p_c(S) = p_o - p_w. \quad (2)$$

Mass conservation for the two incompressible phases gives

$$\phi \partial_t S + \nabla \cdot \mathbf{u}_w = q_w, \quad (3)$$

$$\phi \partial_t (1 - S) + \nabla \cdot \mathbf{u}_o = q_o. \quad (4)$$

The phase fluxes satisfy Darcy’s law,

$$\mathbf{u}_\ell = -\mathbf{K} \lambda_\ell(S) (\nabla p_\ell - \rho_\ell \mathbf{g}), \quad \ell \in \{w, o\}, \quad (5)$$

where

$$\lambda_\ell(S) = \frac{k_{r\ell}(S)}{\mu_\ell} \quad (6)$$

is the phase mobility.

We define the total velocity, total source, total mobility, and wetting-phase fractional-flow function as

$$\mathbf{v} = \mathbf{u}_w + \mathbf{u}_o, \quad (7)$$

$$q_t = q_w + q_o, \quad (8)$$

$$\lambda_t(S) = \lambda_w(S) + \lambda_o(S), \quad (9)$$

$$f(S) = \frac{\lambda_w(S)}{\lambda_t(S)}. \quad (10)$$

Adding Eqs. (3) and (4) gives the total continuity equation

$$\nabla \cdot \mathbf{v} = q_t. \quad (11)$$

A standard way to formulate incompressible two-phase flow is to introduce a global pressure, which absorbs the capillary contribution under the usual global-pressure compatibility assumptions [6, 24]. In the simplified setting relevant to the Buckley–Leverett limit used below, the total velocity can be written as

$$\mathbf{v} = -\mathbf{K} \lambda_t(S) \nabla p_t, \quad (12)$$

where p_t is the global pressure. The corresponding pressure equation is

$$-\nabla \cdot (\mathbf{K} \lambda_t(S) \nabla p_t) = q_t. \quad (13)$$

This pressure equation is not solved in the numerical experiments below; it is included only to place the one-dimensional transport model in the standard two-phase flow setting.

The wetting-phase flux can be expressed in fractional-flow form as

$$\begin{aligned} \mathbf{u}_w = f(S) \mathbf{v} + \mathbf{K} \frac{\lambda_w(S) \lambda_o(S)}{\lambda_t(S)} \nabla p_c(S) \\ - \mathbf{K} \frac{\lambda_w(S) \lambda_o(S)}{\lambda_t(S)} (\rho_o - \rho_w) \mathbf{g}. \end{aligned} \quad (14)$$

Substitution into Eq. (3) yields

$$\phi \partial_t S + \nabla \cdot (f(S)\mathbf{v} + \mathbf{F}_g(S)) = \nabla \cdot \left(\mathbf{K} \frac{\lambda_w(S)\lambda_o(S)}{\lambda_t(S)} \nabla p_c(S) \right) + q_w, \quad (15)$$

with

$$\mathbf{F}_g(S) = -\mathbf{K} \frac{\lambda_w(S)\lambda_o(S)}{\lambda_t(S)} (\rho_o - \rho_w)\mathbf{g}. \quad (16)$$

The computations in this work are restricted to the isothermal, incompressible, one-dimensional Buckley–Leverett limit. Thus capillarity, gravity, and phase sources are neglected in the transport step. Under these assumptions, Eq. (15) reduces to the classical conservation law

$$\phi \partial_t S + \nabla \cdot (f(S)\mathbf{v}) = 0. \quad (17)$$

No thermal energy equation is solved in this work.

B. One-dimensional hyperbolic reduction

We consider a one-dimensional core

$$\Omega = (0, L), \quad (18)$$

with

$$S = S(x, t), \quad \mathbf{v} = (v, 0, 0), \quad (19)$$

where $v > 0$ is constant. Equation (17) then becomes

$$\phi \partial_t S + \partial_x (vf(S)) = 0. \quad (20)$$

Equivalently, after division by the constant porosity ϕ , the equation is written as

$$\partial_t S + \partial_x \mathcal{F}(S) = 0, \quad \mathcal{F}(S) = \frac{v}{\phi} f(S). \quad (21)$$

This is the conservative form discretized by the multiwavelet weak formulation below.

For the hyperbolic problem with $v > 0$, the physical boundary datum is prescribed only at the inflow boundary:

$$S(0, t) = g_D(t). \quad (22)$$

The point $x = L$ is an outflow boundary. No Dirichlet condition is prescribed there in the purely hyperbolic case, because the trace $S(L, t)$ is determined by the interior solution. Imposing an additional Dirichlet value at $x = L$ would overconstrain the first-order hyperbolic problem. If capillarity or another genuinely parabolic regularization is retained, the boundary setting must be enlarged accordingly.

We reserve $f(S)$ for the fractional-flow function and denote the prescribed boundary datum by $g_D(t)$. In the Berea-core computations reported below, the inflow datum is the injected-water saturation,

$$g_D(t) = S_{\text{inj}} = 1 - S_{or}, \quad (23)$$

where S_{or} is the residual oil saturation.

III. FIXED-GRID AFFINE-CONSTRAINED MULTIWAVELET COEFFICIENT FORMULATION

We discretize the one-dimensional conservation law (21) directly in a local orthonormal modal/multiwavelet coefficient space. The formulation is conservative in weak form, so that discontinuities are coupled through numerical interface fluxes rather than through a strong derivative of the reconstructed solution. Its organization is coefficient-space rather than reconstruction-space: boundary traces, cell averages, detail modes, limiting, and affine constraints are all expressed in terms of the local modal coefficients.

The method has three structural features. First, the physical inflow datum is imposed as an affine trace constraint on the coefficient vector. Second, the local basis separates the conservative mean mode from zero-mean detail modes, which provides a natural target for shock limiting. Third, for $p > 1$, the boundary reprojection is applied only to detail coefficients in the inflow cell, so that the imposed trace is recovered without changing the first-cell average. These choices preserve the conservative flux-difference structure on the fixed grid and define the coefficient-space operations validated in the numerical experiments below.

A. Local multiwavelet approximation

Let $\Omega = (0, L)$ be partitioned into N_c cells

$$I_c = (x_{c-1/2}, x_{c+1/2}), \quad (24)$$

$$h_c = x_{c+1/2} - x_{c-1/2}, \quad (25)$$

$$c = 1, \dots, N_c. \quad (26)$$

Each cell is mapped to the reference interval $\widehat{I} = (-1, 1)$ by

$$x = x_c + \frac{h_c}{2}\xi, \quad x_c = \frac{x_{c-1/2} + x_{c+1/2}}{2}, \quad (27)$$

with $\xi \in (-1, 1)$. On \widehat{I} , let $P_k(\xi)$ denote the Legendre polynomial of degree k . The local cell-supported basis used in the implementation is

$$\psi_{c,k}(x) = \left(\frac{2k+1}{h_c} \right)^{1/2} P_k \left(\frac{2(x-x_c)}{h_c} \right), \quad (28)$$

with $k = 0, \dots, p-1$. Here, p denotes the number of local modes per cell; the highest polynomial degree is

therefore $p - 1$. The normalization in Eq. (28) gives the orthonormality relation

$$\int_{I_c} \psi_{c,k}(x) \psi_{c,\ell}(x) dx = \delta_{k\ell}, \quad k, \ell = 0, \dots, p-1. \quad (29)$$

Accordingly, the local mass matrix is the identity,

$$M_{k\ell}^{(c)} = \int_{I_c} \psi_{c,k}(x) \psi_{c,\ell}(x) dx = \delta_{k\ell}, \quad (30)$$

so no local mass inversion is required after assembling the weak residual.

This cellwise orthonormal polynomial representation is used here as a local modal/multiwavelet coefficient representation. The terminology is consistent with piecewise-polynomial multiwavelet constructions, while the conservative weak-form treatment follows the standard structure of high-order discontinuous formulations for conservation laws [25–27]. The important point for the present fixed-grid formulation is the mean/detail coefficient structure: the first mode carries the conservative cell average, whereas the higher modes carry zero-mean local detail information.

The numerical saturation is expanded as

$$S_h(x, t) = \sum_{c=1}^{N_c} \sum_{k=0}^{p-1} s_{c,k}(t) \psi_{c,k}(x), \quad x \in I_c. \quad (31)$$

Equivalently, on a fixed cell,

$$S_h|_{I_c}(x, t) = \sum_{k=0}^{p-1} s_{c,k}(t) \psi_{c,k}(x). \quad (32)$$

The evolved degrees of freedom are therefore the local modal coefficients $s_{c,k}(t)$.

The first basis function is the mean mode. Since $\psi_{c,0} = h_c^{-1/2}$, the cell average is

$$\bar{S}_c(t) = \frac{1}{h_c} \int_{I_c} S_h(x, t) dx = \frac{s_{c,0}(t)}{\sqrt{h_c}}. \quad (33)$$

All higher modes have zero cell average,

$$\int_{I_c} \psi_{c,k}(x) dx = 0, \quad k = 1, \dots, p-1, \quad (34)$$

and therefore represent local detail coefficients. Hence

$$S_h|_{I_c}(x, t) = \bar{S}_c(t) + S'_c(x, t), \quad (35)$$

where

$$\int_{I_c} S'_c(x, t) dx = 0, \quad (36)$$

and

$$S'_c(x, t) = \sum_{k=1}^{p-1} s_{c,k}(t) \psi_{c,k}(x). \quad (37)$$

This mean/detail split is central to the method. The mean coefficient carries the finite-volume-like conservative quantity, while the higher coefficients carry subcell information that can be limited selectively near shocks. This mean/detail structure is also the natural coefficient organization for future adaptive multiresolution extensions, although no adaptive refinement is used in the computations reported here.

Because the basis is supported cellwise, S_h is generally discontinuous at cell interfaces. The left and right traces on cell I_c are

$$S_{c-1/2}^+(t) = \sum_{k=0}^{p-1} s_{c,k}(t) \psi_{c,k}(x_{c-1/2}^+), \quad (38)$$

$$S_{c+1/2}^-(t) = \sum_{k=0}^{p-1} s_{c,k}(t) \psi_{c,k}(x_{c+1/2}^-). \quad (39)$$

Using $P_k(1) = 1$ and $P_k(-1) = (-1)^k$, the trace values of the basis are

$$\psi_{c,k}(x_{c+1/2}^-) = \left(\frac{2k+1}{h_c} \right)^{1/2}, \quad (40)$$

$$\psi_{c,k}(x_{c-1/2}^+) = (-1)^k \left(\frac{2k+1}{h_c} \right)^{1/2}. \quad (41)$$

These traces enter both the numerical interface fluxes and the coefficient-space inflow constraint. In particular, at the left boundary $x = 0 = x_{1-1/2}$, the prescribed inflow condition becomes a linear constraint on the coefficients of the first cell.

Volume integrals are evaluated by Gauss–Legendre quadrature. If $\{\xi_q, w_q\}_{q=1}^Q$ are the quadrature nodes and weights on $(-1, 1)$, then

$$x_{c,q} = x_c + \frac{h_c}{2} \xi_q, \quad w_{c,q} = \frac{h_c}{2} w_q. \quad (42)$$

For a nonlinear function $G(S_h)$, we use

$$\int_{I_c} G(S_h(x, t)) \psi_{c,k}(x) dx \approx \sum_{q=1}^Q w_{c,q} G(S_h(x_{c,q}, t)) \psi_{c,k}(x_{c,q}). \quad (43)$$

The same quadrature nodes are used to evaluate the nonlinear fractional-flow flux in the volume term and to monitor saturation bounds inside each cell.

In the implementation, the values of $\psi_{c,k}(x_{c,q})$, $\partial_x \psi_{c,k}(x_{c,q})$, and the left and right trace vectors are precomputed. Residual assembly therefore consists of coefficient-to-node evaluation, pointwise flux evaluation, projection of the volume term back to coefficient space, and conservative coupling through interface fluxes. This local modal/multiwavelet coefficient structure enables the combination of coefficient-space boundary enforcement, conservative flux coupling, and detail-selective limiting used in the following subsections.

B. Conservative weak residual

The equation discretized in the computations is the scalar conservation law

$$\partial_t S + \partial_x \mathcal{F}(S) = 0, \quad \mathcal{F}(S) = \frac{v}{\phi} f(S), \quad (44)$$

$$\frac{d}{dt} \int_{I_c} S_h(x, t) \psi_{c,k}(x) dx = \int_{I_c} \mathcal{F}(S_h(x, t)) \partial_x \psi_{c,k}(x) dx - \widehat{\mathcal{F}}_{c+1/2} \psi_{c,k}(x_{c+1/2}^-) + \widehat{\mathcal{F}}_{c-1/2} \psi_{c,k}(x_{c-1/2}^+). \quad (45)$$

Here $\widehat{\mathcal{F}}_{c\pm 1/2}$ are numerical fluxes at cell interfaces. They replace the generally double-valued physical flux $\mathcal{F}(S_h)$ at discontinuities of the cellwise representation and provide the conservative coupling between neighboring coefficient blocks.

Using the orthonormality relation (29), the left-hand side of Eq. (45) is simply $ds_{c,k}/dt$. Therefore the coefficient residual is

$$\frac{ds_{c,k}}{dt} = R_{c,k}(\mathbf{s}), \quad (46)$$

with

$$R_{c,k}(\mathbf{s}) = V_{c,k}(\mathbf{s}) - \widehat{\mathcal{F}}_{c+1/2} \psi_{c,k}(x_{c+1/2}^-) + \widehat{\mathcal{F}}_{c-1/2} \psi_{c,k}(x_{c-1/2}^+), \quad (47)$$

where the volume contribution is

$$V_{c,k}(\mathbf{s}) = \int_{I_c} \mathcal{F}(S_h(x, t)) \partial_x \psi_{c,k}(x) dx. \quad (48)$$

In the implementation, this integral is evaluated by the same Gauss–Legendre quadrature used in Eq. (43):

$$V_{c,k}(\mathbf{s}) \approx \sum_{q=1}^Q w_{c,q} \mathcal{F}(S_h(x_{c,q}, t)) \partial_x \psi_{c,k}(x_{c,q}). \quad (49)$$

Thus residual assembly consists of evaluating S_h at quadrature points, computing the nonlinear flux pointwise, projecting the volume term against $\partial_x \psi_{c,k}$, and adding the conservative interface flux contributions.

At an internal interface $x_{c+1/2}$, the numerical flux depends on the left and right traces

$$S_{c+1/2}^- = S_h(x_{c+1/2}^-, t), \quad (50)$$

$$S_{c+1/2}^+ = S_h(x_{c+1/2}^+, t). \quad (51)$$

We write

$$\widehat{\mathcal{F}}_{c+1/2} = \widehat{\mathcal{F}}(S_{c+1/2}^-, S_{c+1/2}^+), \quad (52)$$

where $f(S) = \lambda_w(S)/[\lambda_w(S) + \lambda_o(S)]$ is the wetting-phase fractional-flow function. The discretization follows the weak conservative structure used in high-order discontinuous formulations for hyperbolic conservation laws [26, 28]. In the present formulation, however, the residual is assembled and evolved directly in the local modal/multiwavelet coefficient space introduced above.

For each cell I_c and local basis function $\psi_{c,k}$, $k = 0, \dots, p-1$, multiplication of Eq. (44) by $\psi_{c,k}$, integration over I_c , and integration by parts give

where $\widehat{\mathcal{F}}$ is consistent,

$$\widehat{\mathcal{F}}(S, S) = \mathcal{F}(S). \quad (53)$$

In the production Berea-core calculations reported in Sec. IV, we use the Rusanov flux [29],

$$\widehat{\mathcal{F}}_{c+1/2}^{\text{Rus}} = \frac{1}{2} \left[\mathcal{F}(S_{c+1/2}^-) + \mathcal{F}(S_{c+1/2}^+) \right] - \frac{\alpha_{c+1/2}}{2} (S_{c+1/2}^+ - S_{c+1/2}^-), \quad (54)$$

where

$$\alpha_{c+1/2} \geq \max_{S \in I(S_{c+1/2}^-, S_{c+1/2}^+)} |\mathcal{F}'(S)|. \quad (55)$$

Here $I(S_L, S_R)$ denotes the closed interval with endpoints S_L and S_R . In the numerical experiments below, we use the global admissible-speed bound

$$\alpha_{c+1/2} = a_{\max} = \max_{S \in [S_{wc,1} - S_{or}]} |\mathcal{F}'(S)|, \quad (56)$$

which provides a robust dissipative baseline over the physical saturation interval. The Rusanov flux is commonly used as a local Lax–Friedrichs-type flux in finite-volume and discontinuous Galerkin discretizations of hyperbolic problems.

The implementation also permits a sampled Godunov flux [30]. For a scalar flux, this can be written as

$$\widehat{\mathcal{F}}^{\text{God}}(S_L, S_R) = \begin{cases} \min_{S \in [S_L, S_R]} \mathcal{F}(S), & S_L \leq S_R, \\ \max_{S \in [S_R, S_L]} \mathcal{F}(S), & S_L > S_R. \end{cases} \quad (57)$$

In the code, the extrema are evaluated by sampling the admissible saturation interval. The sampled Godunov flux is used in Sec. IV C to quantify the accuracy–cost tradeoff relative to the Rusanov baseline.

The boundary fluxes are treated consistently with the hyperbolic character of the problem. For $v > 0$, the left

boundary is an inflow boundary and uses the prescribed injected saturation,

$$\widehat{\mathcal{F}}_{1/2} = \widehat{\mathcal{F}}\left(S_{\text{inj}}, S_{1/2}^+\right). \quad (58)$$

The right boundary is an outflow boundary; no Dirichlet value is imposed there. The corresponding numerical flux is evaluated from the interior trace,

$$\widehat{\mathcal{F}}_{N_c+1/2} = \mathcal{F}(S_{N_c+1/2}^-), \quad (59)$$

or equivalently by a consistent numerical flux with identical left and right states.

The conservative structure is seen by choosing the mean mode $k = 0$. Since $\partial_x \psi_{c,0} = 0$ and $\psi_{c,0} = h_c^{-1/2}$, Eq. (45) gives

$$\frac{d\overline{S}_c}{dt} = -\frac{1}{h_c} \left(\widehat{\mathcal{F}}_{c+1/2} - \widehat{\mathcal{F}}_{c-1/2} \right). \quad (60)$$

Thus the mean coefficients obey an exactly conservative flux-difference update, while the higher detail modes evolve through the same weak residual. Summing

Eq. (60) over all cells gives the global balance

$$\frac{d}{dt} \sum_{c=1}^{N_c} h_c \overline{S}_c = -\widehat{\mathcal{F}}_{N_c+1/2} + \widehat{\mathcal{F}}_{1/2}. \quad (61)$$

All internal numerical fluxes cancel pairwise. Therefore conservation is lost neither through the local modal/multiwavelet representation nor through the discontinuity of S_h at interfaces; the only contributions to the global mass balance are the physical inflow and outflow fluxes.

C. Affine enforcement of the inflow condition

For $v > 0$, the one-dimensional Buckley–Leverett problem has a single physical Dirichlet datum, namely the inflow trace

$$S(0, t) = g_D(t). \quad (62)$$

No Dirichlet value is imposed at $x = L$, because the right boundary is an outflow boundary and its trace is determined by the interior solution. In a standard discontinuous weak formulation, boundary data enter through traces and numerical fluxes [26, 27]. Here, in addition, the prescribed inflow trace is enforced algebraically as a linear constraint on the local modal/multiwavelet coefficient vector. Thus the admissible numerical states form an affine subspace of coefficient space.

Let the global coefficient vector be ordered as

$$\mathbf{s}(t) = (s_{1,0}, \dots, s_{1,p-1}, s_{2,0}, \dots, s_{2,p-1}, \dots, s_{N_c,0}, \dots, s_{N_c,p-1})^\top. \quad (63)$$

The left trace is a linear functional of \mathbf{s} :

$$S_h(0^+, t) = \mathbf{m}^\top \mathbf{s}(t). \quad (64)$$

Only the entries associated with the first cell are nonzero. Using Eq. (41), one has

$$m_{1,k} = \psi_{1,k}(x_{1/2}^+) = (-1)^k \left(\frac{2k+1}{h_1} \right)^{1/2}, \quad (65)$$

with $k = 0, \dots, p-1$, and $m_{c,k} = 0$ for $c > 1$. Hence the inflow condition is

$$\mathbf{m}^\top \mathbf{s}(t) = g_D(t). \quad (66)$$

Equivalently, with the row matrix $\mathbf{M} = \mathbf{m}^\top$,

$$\mathbf{M} \mathbf{s}(t) = \mathbf{g}(t), \quad (67)$$

where, for the present scalar inflow condition, $\mathbf{g}(t) = g_D(t)$.

The admissible coefficient vectors form the affine space

$$\mathcal{A}_g(t) = \{ \mathbf{s} : \mathbf{M} \mathbf{s} = \mathbf{g}(t) \}. \quad (68)$$

A standard constrained parametrization is obtained by choosing a lifting vector $\boldsymbol{\ell}(t)$ such that

$$\mathbf{M} \boldsymbol{\ell}(t) = \mathbf{g}(t), \quad (69)$$

and writing

$$\mathbf{s}(t) = \boldsymbol{\ell}(t) + \mathbf{z}(t), \quad \mathbf{M} \mathbf{z}(t) = 0. \quad (70)$$

If the columns of \mathbf{Z} span $\ker \mathbf{M}$, then

$$\mathbf{z}(t) = \mathbf{Z} \mathbf{y}(t), \quad \mathbf{s}(t) = \boldsymbol{\ell}(t) + \mathbf{Z} \mathbf{y}(t), \quad (71)$$

where $\mathbf{y}(t)$ is an unconstrained reduced coefficient vector.

Let the conservative residual generated by Eq. (45) be

$$\frac{d\mathbf{s}}{dt} = \mathcal{R}(\mathbf{s}). \quad (72)$$

Substitution of Eq. (71) gives

$$\mathbf{Z} \frac{d\mathbf{y}}{dt} = \mathcal{R}(\boldsymbol{\ell} + \mathbf{Z}\mathbf{y}) - \frac{d\boldsymbol{\ell}}{dt}. \quad (73)$$

Projection onto the homogeneous trace space gives

$$\frac{d\mathbf{y}}{dt} = \mathbf{Z}^\dagger \left[\mathcal{R}(\boldsymbol{\ell} + \mathbf{Z}\mathbf{y}) - \frac{d\boldsymbol{\ell}}{dt} \right], \quad (74)$$

where \mathbf{Z}^\dagger is the left inverse associated with the chosen coefficient inner product. If the columns of \mathbf{Z} are orthonormal in this inner product, then $\mathbf{Z}^\dagger = \mathbf{Z}^\top$.

In the implementation, \mathbf{Z} is not formed explicitly. Since there is only one scalar inflow constraint, an equivalent correction can be applied directly to the coefficient vector. For an arbitrary coefficient vector \mathbf{s} , define the trace defect

$$d_g(\mathbf{s}) = g_D(t) - \mathbf{m}^\top \mathbf{s}. \quad (75)$$

The full minimum-norm affine correction is

$$\mathcal{P}_{\mathcal{A}_g}^{\text{full}} \mathbf{s} = \mathbf{s} + \frac{d_g(\mathbf{s})}{\mathbf{m}^\top \mathbf{m}} \mathbf{m}. \quad (76)$$

Indeed,

$$\mathbf{m}^\top \mathcal{P}_{\mathcal{A}_g}^{\text{full}} \mathbf{s} = \mathbf{m}^\top \mathbf{s} + d_g(\mathbf{s}) = g_D(t), \quad (77)$$

so $\mathcal{P}_{\mathcal{A}_g}^{\text{full}} \mathbf{s} \in \mathcal{A}_g(t)$.

A full correction enforces the trace, but it may also change the mean coefficient of the inflow cell. For the production calculations with $p > 1$, we therefore use a detail-only affine correction. Let \mathbf{m}_d collect the trace values of the nonzero detail modes $k = 1, \dots, p-1$ in the first cell, and let $\mathbf{s}_{1,d}$ denote the corresponding detail coefficients. The detail-only correction is

$$\mathbf{s}_{1,d}^{\text{new}} = \mathbf{s}_{1,d}^{\text{old}} + \frac{g_D(t) - \mathbf{m}^\top \mathbf{s}^{\text{old}}}{\mathbf{m}_d^\top \mathbf{m}_d} \mathbf{m}_d. \quad (78)$$

The mean coefficient $s_{1,0}$ is left unchanged. Thus, for $p > 1$, the affine reprojection restores the inflow trace without modifying the conservative cell-average update in the inflow cell. For $p = 1$, no detail subspace is available, and the implementation falls back to the full correction in Eq. (76).

The same projection idea is applied to the residual. To keep the semidiscrete velocity tangent to the homogeneous constraint, we remove the component of \mathcal{R} in the full trace direction:

$$\mathcal{R}_{\text{tan}}(\mathbf{s}) = \mathcal{R}(\mathbf{s}) - \frac{\mathbf{m}^\top \mathcal{R}(\mathbf{s})}{\mathbf{m}^\top \mathbf{m}} \mathbf{m}. \quad (79)$$

Consequently,

$$\mathbf{m}^\top \mathcal{R}_{\text{tan}}(\mathbf{s}) = 0. \quad (80)$$

Thus the residual update is tangent to the homogeneous constraint manifold. The affine correction is nevertheless reimposed after each Runge–Kutta stage to remove

roundoff-level drift and to ensure that the limited state remains compatible with the prescribed trace. For $p > 1$, this stage reprojection uses the detail-only correction in Eq. (78). This choice preserves the mean coefficient of the inflow cell and therefore does not alter the conservative cell-average update. It should be distinguished from a pointwise bound projection: the detail-only trace correction enforces the boundary trace under a fixed cell average, and therefore pointwise boundedness of all monitored points inside the constrained inflow cell is not guaranteed after the final reprojection.

For the Berea-core computations,

$$g_D(t) = S_{\text{inj}} = 1 - S_{\text{or}} \quad (81)$$

is constant. Hence $d\boldsymbol{\ell}/dt = 0$, and the role of the affine lifting is to keep the left trace equal to the injected-water saturation throughout the conservative coefficient evolution. The right boundary is not included in \mathbf{M} ; it is treated as an outflow boundary through the numerical flux in Eq. (59).

D. Limiter and bound preservation

The conservative residual (45) gives the correct cell-average flux balance, but higher modal/detail coefficients must be controlled near entropy shocks. We therefore apply a local limiting procedure after each stage of the strong-stability-preserving Runge–Kutta update. The construction follows the standard logic of local projection limiting for discontinuous Galerkin conservation-law discretizations and maximum-principle-preserving rescaling for scalar conservation laws [28, 31, 32].

Using the mean/detail decomposition (35), the limiter acts on the zero-mean component S'_c . Hence the cell average \bar{S}_c , and therefore the conservative mean update generated by Eq. (45), is not changed by the detail limiting step. This is the coefficient-space analogue of preserving finite-volume cell averages while suppressing only the oscillatory subcell content responsible for nonphysical oscillations near shocks.

Troubled cells are identified from the reconstructed interface traces. Let

$$S_c^- = S_h(x_{c-1/2}^+, t), \quad S_c^+ = S_h(x_{c+1/2}^-, t), \quad (82)$$

and define the neighboring average jumps

$$\Delta_c^- = \bar{S}_c - \bar{S}_{c-1}, \quad \Delta_c^+ = \bar{S}_{c+1} - \bar{S}_c. \quad (83)$$

A cell is flagged when the deviation of either trace from the cell average is not compatible with the limited one-sided differences. Specifically, we compare

$$S_c^+ - \bar{S}_c \quad \text{with} \quad \min\text{mod}(S_c^+ - \bar{S}_c, \beta \Delta_c^-, \beta \Delta_c^+), \quad (84)$$

and

$$\bar{S}_c - S_c^- \quad \text{with} \quad \min\text{mod}(\bar{S}_c - S_c^-, \beta \Delta_c^-, \beta \Delta_c^+). \quad (85)$$

Here $1 \leq \beta \leq 2$ is a sensitivity parameter, and

$$\min\text{mod}(a_1, \dots, a_m) = \begin{cases} \text{sgn}(a_1) \min_{1 \leq j \leq m} |a_j|, & \text{if } \text{sgn}(a_1) = \dots = \text{sgn}(a_m), \\ 0, & \text{otherwise.} \end{cases} \quad (86)$$

Smooth cells are left unchanged by the troubled-cell limiter. In troubled cells, the zero-mean detail part is rescaled according to

$$S_h^{\text{lim}}(x, t)|_{I_c} = \bar{S}_c(t) + \theta_c S'_c(x, t), \quad 0 \leq \theta_c \leq 1. \quad (87)$$

The rescaling parameter is then chosen to enforce the admissible saturation interval at the quadrature and interface points used by the scheme.

The admissible bounds are

$$S_{\min} = S_{wc}, \quad S_{\max} = 1 - S_{or}. \quad (88)$$

Let

$$S_c^{\max} = \max_{x_q \in I_c} S_h(x_q, t), \quad S_c^{\min} = \min_{x_q \in I_c} S_h(x_q, t), \quad (89)$$

where the set of points includes the quadrature nodes used for volume integration and the two cell interfaces. The bound-preserving rescaling parameter is chosen as

$$\theta_c = \min \left\{ 1, \frac{S_{\max} - \bar{S}_c}{S_c^{\max} - \bar{S}_c + \varepsilon}, \frac{\bar{S}_c - S_{\min}}{\bar{S}_c - S_c^{\min} + \varepsilon} \right\}, \quad (90)$$

with a small $\varepsilon > 0$ to avoid division by zero. If the reconstructed polynomial already lies in the admissible interval at the monitored points, then $\theta_c = 1$. If not, only the zero-mean detail part is reduced.

For every monitored point $x_q \in I_c$, namely every quadrature or interface point used by the scheme, the limited value is

$$S_h^{\text{lim}}(x_q, t) = \bar{S}_c + \theta_c (S_h(x_q, t) - \bar{S}_c). \quad (91)$$

Therefore, by construction,

$$S_{wc} \leq S_h^{\text{lim}}(x_q, t) \leq 1 - S_{or} \quad \text{at all monitored points.} \quad (92)$$

At the same time,

$$\frac{1}{|I_c|} \int_{I_c} S_h^{\text{lim}}(x, t) dx = \bar{S}_c, \quad (93)$$

because S'_c has zero mean. Thus the limiter enforces the physical bounds at the points used by the scheme without altering the conservative cell-average evolution.

After limiting and bound enforcement, the coefficient vector is returned to the affine constraint space associated with the imposed inflow trace. For $p > 1$, the production

implementation uses the detail-only affine correction introduced in Eq. (78). This restores the prescribed trace without changing the first-cell average. For $p = 1$, no detail subspace is available, and the code falls back to the full minimum-norm trace correction in Eq. (76).

Consequently, every Runge–Kutta stage returns a coefficient vector that satisfies the prescribed inflow trace and preserves the conservative cell-average update under detail limiting for $p > 1$. The bound-preserving rescaling enforces the admissible saturation interval at the monitored quadrature and interface points before the final affine reprojection. In the constrained inflow cell, the final detail-only reprojection may move some monitored values outside the admissible interval because the imposed boundary trace and the preserved first-cell average are enforced simultaneously. In the flux evaluation, saturation arguments are clipped to the physical interval, and the trace and mass-balance diagnostics are therefore reported separately in Sec. IV.

E. Time integration and CFL condition

After the spatial discretization in Eq. (45), the cellwise modal/multiwavelet coefficients satisfy the semidiscrete system

$$\frac{ds}{dt} = \mathcal{R}_{\text{tan}}(s), \quad (94)$$

where \mathcal{R}_{tan} is the conservative residual projected onto the tangent space of the inflow constraint, as defined in Eq. (79). The affine trace constraint is reimposed after every Runge–Kutta stage to remove roundoff-level drift and to return the stage value to the admissible coefficient space.

The coefficient system is advanced by the third-order strong-stability-preserving Runge–Kutta method [32]. For one step from t^n to $t^{n+1} = t^n + \Delta t$, the uncleaned stage updates are

$$\mathbf{s}^{(1)} = \mathbf{s}^n + \Delta t \mathcal{R}_{\text{tan}}(\mathbf{s}^n), \quad (95)$$

$$\mathbf{s}^{(2)} = \frac{3}{4} \mathbf{s}^n + \frac{1}{4} \left[\mathbf{s}^{(1)} + \Delta t \mathcal{R}_{\text{tan}}(\mathbf{s}^{(1)}) \right], \quad (96)$$

$$\mathbf{s}^{n+1} = \frac{1}{3} \mathbf{s}^n + \frac{2}{3} \left[\mathbf{s}^{(2)} + \Delta t \mathcal{R}_{\text{tan}}(\mathbf{s}^{(2)}) \right]. \quad (97)$$

After each intermediate stage and after the final stage, the updated state is processed by the nonlinear cleaning

sequence

$$\mathbf{s} \mapsto \Pi_{\mathcal{A}_g} \mathcal{L}_{\text{TVB}} \mathcal{B} \Pi_{\mathcal{A}_g}(\mathbf{s}). \quad (98)$$

Here $\Pi_{\mathcal{A}_g}$ denotes projection onto the affine trace space

$$\mathcal{A}_g = \{\mathbf{s} : \mathbf{M}\mathbf{s} = \mathbf{g}\}, \quad (99)$$

\mathcal{B} denotes the mean-preserving bound rescaling in Eq. (90), and \mathcal{L}_{TVB} denotes the TVB/minmod troubled-cell correction. The first projection enforces the inflow trace before limiting. The bound-rescaling step then reduces zero-mean detail content when the reconstructed saturation exceeds the admissible interval at the monitored quadrature and interface points. The TVB/minmod step further regularizes troubled cells near shocks. The final projection restores the affine inflow trace after these nonlinear limiting operations.

For $p > 1$, the final projection is the detail-only correction in Eq. (78); for $p = 1$, it reduces to the full minimum-norm correction in Eq. (76). Thus every intermediate and final Runge–Kutta state satisfies the prescribed inflow trace. The mean-preserving bound rescaling controls the monitored saturation values before the subsequent TVB/minmod and affine reprojection steps. Since the final detail-only projection enforces the inflow trace by modifying detail coefficients in the constrained inflow cell, pointwise boundedness in that cell is monitored numerically rather than guaranteed analytically at every stage.

The time step is chosen from a Courant–Friedrichs–Lewy restriction [33]. For the scalar conservation law

$$\partial_t S + \partial_x \mathcal{F}(S) = 0, \quad (100)$$

the characteristic speed is

$$a(S) = \mathcal{F}'(S) = \frac{v}{\phi} f'(S). \quad (101)$$

We use the global admissible-speed bound

$$\begin{aligned} a_{\max} &= \max_{S \in [S_{wc}, 1 - S_{or}]} |a(S)| \\ &= \frac{|v|}{\phi} \max_{S \in [S_{wc}, 1 - S_{or}]} |f'(S)|. \end{aligned} \quad (102)$$

For p local modes per cell, the computations use the explicit time step

$$\Delta t = C_{\text{CFL}} \frac{\Delta x_{\min}}{(2p + 1)a_{\max}}, \quad (103)$$

where $\Delta x_{\min} = \min_c |I_c|$. The factor $2p + 1$ is the degree-dependent scaling used here for the explicit high-order discontinuous transport update, and it becomes more restrictive as the number of local modes is increased. In the Berea-core simulations reported below, $p = 2$ and $C_{\text{CFL}} = 0.20$. The dependence on p is examined separately in Sec. IV C. The same time-step restriction is used for residual evaluation, limiting, and affine trace reprojection throughout the Runge–Kutta stages.

IV. NUMERICAL VALIDATION

We validate the conservative affine-constrained multi-wavelet coefficient method on a one-dimensional Berea-core Buckley–Leverett displacement benchmark. The tests are designed to assess the coefficient-space mechanisms introduced in Sec. III: direct evolution of local modal/multiwavelet coefficients, conservative interface-flux coupling, affine enforcement of the inflow trace, detail-only boundary reprojection for $p > 1$, troubled-cell limiting, and preservation of admissible saturation bounds at the quadrature and interface points used by the scheme.

The reference solution is computed independently with `pywaterflood`, using the same physical parameters, fractional-flow closure, and pore-volume-injected scaling [23]. The solver used in this work was implemented directly in Python. The local orthonormal modal/multiwavelet basis, coefficient-to-node evaluation, conservative weak residual, numerical interface fluxes, affine boundary lifting, detail limiting, diagnostics, and explicit time stepping were all implemented in the present code.

All computations reported here are performed on fixed uniform meshes. The numerical study therefore focuses on the conservative coefficient-space mechanisms themselves: affine inflow enforcement, detail-only boundary reprojection, mean/detail limiting, monotone flux coupling, and mass-balance preservation. Dynamic mesh refinement, coefficient thresholding, and sparse adaptive operator representations are left for future extensions.

A. Computational setup

The Berea core has length and diameter

$$L = 6.0 \text{ in} = 0.1524 \text{ m}, \quad D = 1.5 \text{ in} = 0.0381 \text{ m}, \quad (104)$$

with cross-sectional area $A = \pi D^2/4$. The imposed injection rate is $q = 1.0 \text{ mL/min}$, giving the Darcy velocity $v = q/A$. The porosity and residual saturations are

$$\phi = 0.20, \quad S_{wc} = 0.10, \quad S_{or} = 0.20. \quad (105)$$

Thus the initial and injected saturations are

$$S(x, 0) = S_{wc} = 0.10, \quad S(0, t) = S_{\text{inj}} = 1 - S_{or} = 0.80. \quad (106)$$

The phase viscosities are

$$\mu_w = 1.0 \times 10^{-3} \text{ Pa}\cdot\text{s}, \quad \mu_o = 4.0 \times 10^{-3} \text{ Pa}\cdot\text{s}. \quad (107)$$

For the Berea benchmark, the relative permeabilities are modeled by Corey laws. The effective water saturation is

$$S_e = \frac{S - S_{wc}}{1 - S_{wc} - S_{or}}, \quad 0 \leq S_e \leq 1, \quad (108)$$

and the relative permeabilities are

$$k_{rw}(S) = k_{rw}^0 S_e^{n_w}, \quad (109)$$

$$k_{ro}(S) = k_{ro}^0 (1 - S_e)^{n_o}. \quad (110)$$

In the computations reported here,

$$k_{rw}^0 = k_{ro}^0 = 1, \quad n_w = n_o = 2. \quad (111)$$

The phase mobilities are

$$\lambda_w(S) = \frac{k_{rw}(S)}{\mu_w}, \quad \lambda_o(S) = \frac{k_{ro}(S)}{\mu_o}, \quad (112)$$

and the water fractional flow is

$$f(S) = \frac{\lambda_w(S)}{\lambda_w(S) + \lambda_o(S)}. \quad (113)$$

During flux evaluation and limiting, S_e is clipped to $[0, 1]$, so that the computed saturation remains in the physical interval

$$S_{wc} \leq S \leq 1 - S_{or}. \quad (114)$$

The results are reported in terms of pore volumes injected. The pore volume of the core is $V_p = \phi AL$, and the dimensionless injected pore volume is

$$\text{PVI}(t) = \frac{qt}{\phi AL}. \quad (115)$$

Thus one pore volume corresponds to $t_{PV} = \phi AL/q$. The same fractional-flow function, physical parameters, initial condition, inflow saturation, and pore-volume scaling are used in the multiwavelet coefficient solver and in the `pywaterflood` reference calculation.

Unless otherwise stated, the simulations use a uniform partition with $N_c = 256$ cells, $p = 2$ local modes per cell, the Rusanov numerical flux, and the troubled-cell limiter described in Sec. III D. Here $p = 2$ corresponds to a piecewise-linear local modal representation. This choice is used as the main production setting because the modal-order sensitivity study in Sec. IV C shows that it gives the best accuracy–cost compromise among the tested orders for the present shock-dominated benchmark. The time step is chosen from the CFL condition in Eq. (103) with $C_{\text{CFL}} = 0.20$. The affine trace condition is reimposed after every Runge–Kutta stage.

B. Breakthrough, profiles, and error measures

Figure 1 compares the breakthrough behavior at the midpoint of the core,

$$x_p = L/2 = 7.62 \text{ cm}. \quad (116)$$

Before the arrival of the displacement front, both solutions remain at the initial connate-water saturation. After breakthrough, the affine-constrained multiwavelet

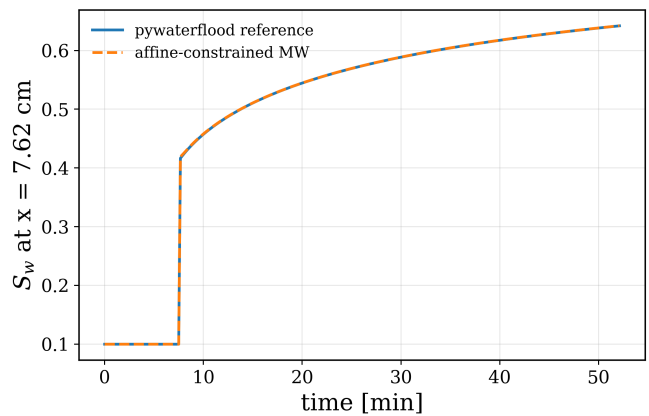


FIG. 1. Breakthrough curve for the Berea-core Buckley–Leverett benchmark at $x = L/2 = 7.62$ cm. The affine-constrained multiwavelet coefficient solution computed with $N_c = 256$, $p = 2$, and Rusanov flux is compared with the `pywaterflood` reference solution using the same Corey fractional-flow parameters and pore-volume-injected scaling.

coefficient solution captures the rapid increase in water saturation and its subsequent approach toward the injected state. The agreement of the two curves shows that the conservative interface fluxes propagate the nonlinear Buckley–Leverett front at the correct speed while the affine constraint maintains the prescribed inflow saturation.

Figure 2 compares water-saturation profiles along the core at selected pore volumes injected. The affine-constrained multiwavelet coefficient solution captures the advancing displacement front without visible undershoots below S_{wc} or overshoots above $1 - S_{or}$. The profiles remain close to the reference solution both near the sharp displacement front and in the smoother post-front saturation region. This comparison also illustrates the role of the troubled-cell limiter: smooth regions retain the local modal representation, whereas cells near the shock are locally regularized without changing their cell averages.

For quantitative comparisons, let S_i^{MW} denote the affine-constrained coefficient solution sampled at the cell centers and S_i^{ref} the corresponding reference value. We report the root-mean-square error

$$E_{\text{RMSE}} = \left[\frac{1}{N} \sum_{i=1}^N (S_i^{\text{MW}} - S_i^{\text{ref}})^2 \right]^{1/2}, \quad (117)$$

and the maximum pointwise error

$$E_{\infty} = \max_i |S_i^{\text{MW}} - S_i^{\text{ref}}|. \quad (118)$$

Because the solution contains a sharp saturation front, E_{∞} is especially sensitive to small differences in front location, whereas E_{RMSE} gives a more global measure of profile agreement.

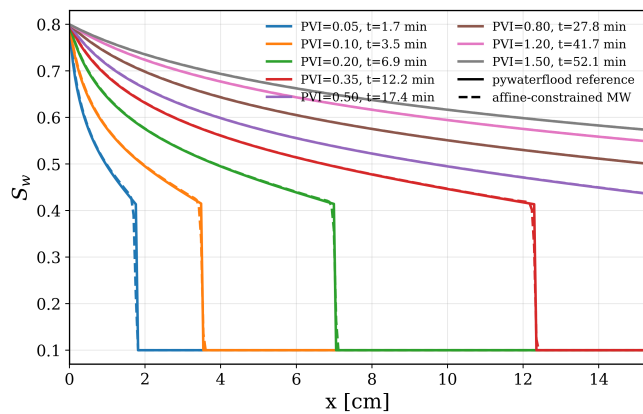


FIG. 2. Water-saturation profiles for the Berea-core Buckley–Leverett benchmark at selected pore volumes injected. The affine-constrained multiwavelet coefficient solution computed with $N_c = 256$, $p = 2$, and Rusanov flux is compared with the `pywaterflood` reference solution. The profiles show conservative front propagation, control of saturation bounds by the detail limiter, and enforcement of the injected-water state at the inflow boundary.

TABLE I. Profile errors between the affine-constrained multiwavelet coefficient solution and the `pywaterflood` reference solution at selected pore volumes injected. The calculation uses $N_c = 256$, $p = 2$, and the Rusanov flux.

| PVI | E_{RMSE} | E_{∞} |
|------|-------------------------|--------------------------|
| 0.05 | 1.2358×10^{-2} | 1.94526×10^{-1} |
| 0.10 | 5.2830×10^{-3} | 7.4713×10^{-2} |
| 0.20 | 5.2850×10^{-3} | 6.2596×10^{-2} |
| 0.35 | 5.9430×10^{-3} | 9.0774×10^{-2} |
| 0.50 | 3.8400×10^{-4} | 7.9200×10^{-4} |
| 0.80 | 2.5100×10^{-4} | 4.9400×10^{-4} |
| 1.20 | 1.9700×10^{-4} | 3.2900×10^{-4} |
| 1.50 | 1.7300×10^{-4} | 2.6300×10^{-4} |

Table I reports the profile errors at the same selected pore volumes used in Fig. 2. The largest pointwise errors occur at early pore volumes, when the displacement front is sharp and a small difference in front position produces a large local discrepancy. In this regime, two visually close profiles may still give a large E_{∞} , because the error is evaluated pointwise across a nearly discontinuous transition. After the front has crossed the core, both E_{RMSE} and E_{∞} decrease to the 10^{-4} range.

C. Flux comparison, mesh refinement, and modal-order sensitivity

We next examine the sensitivity of the fixed-grid affine-constrained multiwavelet coefficient solver to the numerical flux, mesh resolution, and number of local modes. These tests verify that the agreement shown in Figs. 1 and 2 is not tied to a single discretization choice. They

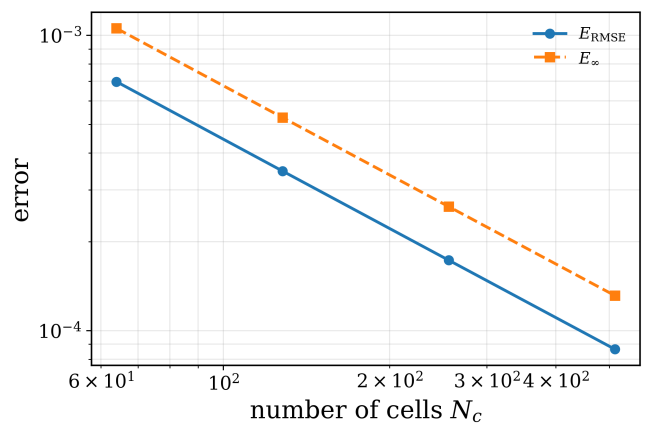


FIG. 3. Mesh-refinement study for the affine-constrained multiwavelet coefficient solver using the Rusanov flux and $p = 2$. Both the root-mean-square error and maximum pointwise error decrease under refinement. The maximum error is dominated by the narrow shock region and is therefore more sensitive to small front-location differences.

also quantify the computational tradeoff between the inexpensive Rusanov flux and the more expensive sampled Godunov flux.

The parameter p denotes the number of local modes per cell. Thus $p = 1$ corresponds to a piecewise-constant representation, $p = 2$ to a piecewise-linear representation, $p = 3$ to a piecewise-quadratic representation, and in general the highest local polynomial degree is $p - 1$. The total number of saturation degrees of freedom is

$$N_{\text{dof}} = N_c p. \quad (119)$$

Because the Buckley–Leverett benchmark contains an entropy shock, the modal-order study should not be interpreted as a formal smooth-solution p -convergence test. In this regime, the global error is controlled by shock localization, numerical-flux dissipation, and the nonlinear action of the troubled-cell and bound-preserving limiters.

Table II compares the Rusanov and sampled Godunov fluxes at fixed $N_c = 256$ and $p = 2$. For this benchmark and modal order, the two monotone fluxes give comparable profile errors, with the Rusanov flux giving slightly smaller reported global errors and substantially lower wall time. The sampled Godunov flux remains useful as a monotone comparison flux, but its additional cost is significant because the local flux extremum is evaluated by sampling the admissible saturation interval. For this reason, the Rusanov flux is used as the main production flux in the remaining tests.

Figure 3 reports the mesh-refinement behavior at fixed $p = 2$ using the Rusanov flux. Both the root-mean-square error and the maximum pointwise error decrease under refinement. The decrease of E_{RMSE} shows systematic improvement of the global saturation profile, while E_{∞} is more sensitive to small differences in front location because the reference profile contains a narrow shock transition.

TABLE II. Flux comparison at $N_c = 256$ and $p = 2$. The sampled Godunov flux and the Rusanov flux give comparable errors for this benchmark, while the Rusanov flux is substantially cheaper in the present implementation.

| Flux | E_{RMSE} | E_∞ | Trace error | Mass defect | Wall time [s] |
|---------|---------------------------|---------------------------|---------------------|-------------------------|---------------|
| Godunov | 1.832240×10^{-4} | 3.012753×10^{-4} | 0.000×10^0 | 1.862×10^{-10} | 429.462 |
| Rusanov | 1.730984×10^{-4} | 2.629553×10^{-4} | 0.000×10^0 | 6.955×10^{-11} | 138.092 |

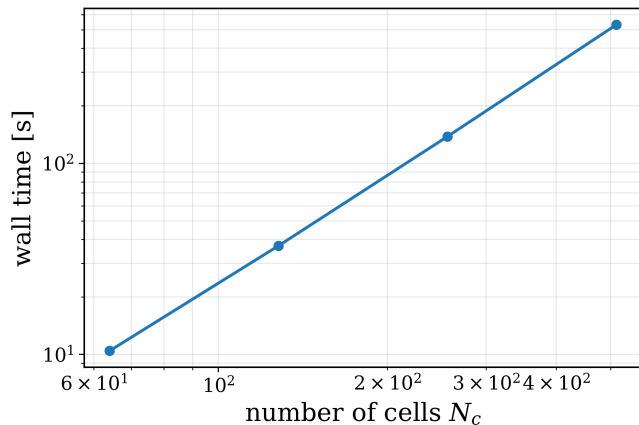


FIG. 4. Runtime scaling for the affine-constrained multiwavelet coefficient solver using the Rusanov flux and $p = 2$. For fixed final physical time, the wall-clock time increases superlinearly with N_c , because refinement increases both the number of degrees of freedom and the number of explicit time steps through the CFL restriction.

The associated wall-clock time is shown in Fig. 4. For a fixed final physical time, the runtime increases superlinearly with N_c , because mesh refinement increases both the number of degrees of freedom and the number of explicit time steps through the CFL condition. The timings are reported for the present Python implementation and are intended to quantify relative cost across the tested discretizations, not optimized parallel scalability.

Table III reports the modal-order sensitivity at fixed $N_c = 256$ using the Rusanov flux. The dependence on p is nonmonotone, as expected for a shock-capturing calculation with nonlinear limiting. In smooth regions, increasing p enriches the local representation. Near the Buckley–Leverett front, however, the error is dominated by front localization and by the interaction between modal detail coefficients and the troubled-cell limiter. In the present benchmark, $p = 2$ gives the most favorable accuracy–cost compromise among the tested modal orders; $p = 4$ gives comparable accuracy at substantially larger runtime, while $p = 3$ is more sensitive to limiter–front interaction.

Finally, we monitor the diagnostics most directly connected with the proposed coefficient-space construction: the imposed inflow trace and the discrete global mass balance. The affine trace constraint is designed to keep the left boundary value fixed at the injected saturation, while the conservative weak residual gives the discrete

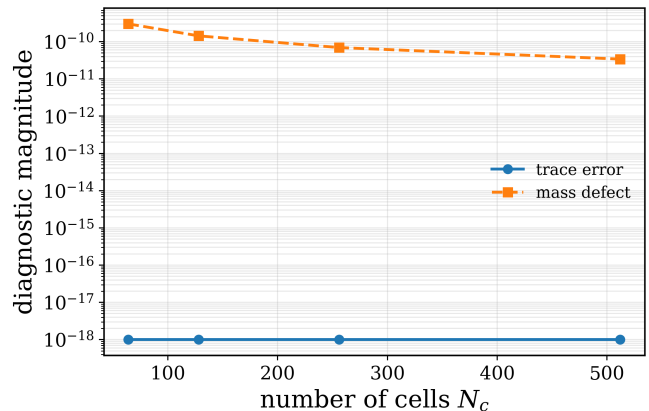


FIG. 5. Boundary-trace and mass-balance diagnostics for the affine-constrained multiwavelet coefficient solver using the Rusanov flux and $p = 2$. The imposed inflow trace is preserved at roundoff level, while the accumulated global mass-balance defect remains small over the refinement study.

global mass balance up to time-integration and quadrature error. These diagnostics are essential because the method combines three nonlinear operations at every Runge–Kutta stage: flux evaluation, detail limiting, and affine trace reprojection.

The trace error is measured as

$$E_{\text{tr}}(t) = |S_h(0, t) - S_{\text{inj}}|, \quad (120)$$

and the accumulated mass-balance defect is computed from the difference between the change in total saturation and the time-integrated net boundary flux,

$$E_M(t) = \left| \int_{\Omega} S_h(x, t) dx - \int_{\Omega} S_h(x, 0) dx + \int_0^t \left[\widehat{\mathcal{F}}_{N_c+1/2}(\tau) - \widehat{\mathcal{F}}_{1/2}(\tau) \right] d\tau \right|. \quad (121)$$

Figure 5 shows that the affine inflow constraint is preserved to roundoff accuracy and that the accumulated mass-balance defect remains small over the refinement study. These diagnostics confirm that the coefficient-space boundary treatment is compatible with the conservative weak residual, even though the stage update combines nonlinear flux evaluation, detail limiting, and affine trace reprojection.

TABLE III. Modal-order sensitivity at fixed $N_c = 256$ using the Rusanov flux. Here p is the number of local modes per cell and the polynomial degree is $p - 1$. Because the solution contains a shock, monotone improvement with increasing p is not expected.

| p | Degree | N_{dof} | N_{steps} | E_{RMSE} | E_{∞} | Wall time [s] |
|-----|--------|------------------|--------------------|---------------------------|---------------------------|---------------|
| 1 | 0 | 256 | 19190 | 9.351175×10^{-3} | 1.405022×10^{-2} | 4.887 |
| 2 | 1 | 512 | 31983 | 1.730984×10^{-4} | 2.629553×10^{-4} | 138.092 |
| 3 | 2 | 768 | 44775 | 1.787295×10^{-3} | 1.687640×10^{-2} | 195.469 |
| 4 | 3 | 1024 | 57568 | 2.395573×10^{-4} | 1.903429×10^{-3} | 251.171 |

V. CONCLUSIONS

We have developed a fixed-grid conservative affine-constrained modal/multiwavelet coefficient method for the one-dimensional Buckley–Leverett saturation equation. The saturation is evolved directly in a local orthonormal coefficient space, and the nonlinear fractional-flow front is advanced through a conservative weak formulation with monotone numerical interface fluxes. The method therefore treats the coefficient representation as the primary discretization space, rather than as a post-processing reconstruction, compression device, or error indicator.

The main contribution is the coefficient-space treatment of the hyperbolic inflow condition. The prescribed inflow trace is imposed as a linear constraint on the coefficient vector and enforced by affine lifting. For $p > 1$, the stage reprojection is applied in the detail subspace of the inflow cell, so that the trace is restored without changing the mean coefficient and hence without altering the conservative cell-average update. Shock-induced oscillations are controlled by a troubled-cell limiter acting on zero-mean detail coefficients, while saturation bounds are controlled by a mean-preserving rescaling at the quadrature and interface points used by the scheme. This construction keeps the boundary constraint, the limiter, and the conservative update in the same coefficient space.

The Berea-core benchmark validates the complete fixed-grid formulation. Using the same Corey fractional-flow closure, physical parameters, and pore-volume-injected scaling as the independent `pywaterflood` reference calculation, the affine-constrained coefficient solver reproduces the breakthrough curve and saturation profiles. The imposed inflow trace is preserved to roundoff accuracy, the accumulated mass-balance defect remains small, and mesh refinement at fixed $p = 2$ reduces the profile errors. The flux and modal-order studies show that the Rusanov flux with $p = 2$ provides the most favorable accuracy–cost compromise among the tested settings for this shock-dominated benchmark.

The present implementation is intentionally fixed-grid. It does not use dynamic mesh refinement, coefficient thresholding, or sparse adaptive operator representations. Its purpose is to establish the conservative coefficient-space ingredients needed before introducing adaptivity: affine inflow enforcement, detail-only trace correction, mean/detail limiting, saturation-bound control, and conservative flux coupling. These validated operations provide a basis for future extensions to hierarchical adaptive meshes, local *hp*-adaptivity, heterogeneous cores, gravity and capillary corrections, and coupled pressure–transport simulations.

DATA AVAILABILITY

The data supporting the findings of this study are available from the corresponding author upon reasonable request. The code used in this work is publicly available at https://github.com/Christian48596/mw_affine_buckley_leverett. The repository contains the Buckley–Leverett multiwavelet solver, the default Berea benchmark settings, and documentation for modifying the rock and fluid parameters. The results reported in this study can be reproduced from the code and input settings provided in that repository.

ACKNOWLEDGMENTS

Ch.T. acknowledges support from the Deanship of Research (DOR) at King Fahd University of Petroleum & Minerals (KFUPM) through project No. EC251017. E.D. acknowledges support from the Research Council of Norway through its Centres of Excellence scheme, Hylleraas Centre, project No. 262695. The authors thank Prof. Dr. Antoine Levitt, Laboratoire de Mathématiques d’Orsay at the Université Paris-Saclay, and Dr. Magnar Bjørgve, UiT The Arctic University of Norway, for useful discussions.

[1] S. E. Buckley and M. C. Leverett, *Mechanism of fluid displacement in sands*, Transactions of the AIME **146**, 107–116 (1942).

[2] S. E. Buckley and M. C. Leverett, *Mechanism of fluid displacements in sands*, Transactions of the AIME **146**, 107–116 (1952), classical work on immiscible two-phase

- displacement theory using fractional flow analysis.
- [3] L. Belazreg, S. M. Mahmood, and A. Aulia, *Novel approach for predicting water alternating gas injection recovery factor*, Journal of Petroleum Exploration and Production Technology **9**, 2893–2910 (2019), forecasting performance of immiscible WAG floods using analytical prediction tools.
 - [4] L. P. Dake, *Fundamentals of Reservoir Engineering*, Developments in Petroleum Science, Vol. 8 (Elsevier, Amsterdam, 1978).
 - [5] R. Helmig, *Multiphase Flow and Transport Processes in the Subsurface: A Contribution to the Modeling of Hydrosystems* (Springer, Berlin Heidelberg, 1997).
 - [6] Z. Chen, G. Huan, and Y. Ma, *Computational Methods for Multiphase Flows in Porous Media* (SIAM, Philadelphia, 2006).
 - [7] E. F. Kaasschieter, *Solving the buckley–leverett equation with gravity in a heterogeneous porous medium*, Computational Geosciences **3**, 23–48 (1999), hyperbolic limit and capillary regularisation discussion.
 - [8] K. R. Spayd, *The buckley–leverett equation with dynamic capillary pressure*, SIAM Journal on Applied Mathematics **71**, 1275–1300 (2011), shows how the Buckley–Leverett model becomes pseudo-parabolic when a dynamic capillary term is included, and reduces to a hyperbolic conservation law in the capillarity-free limit.
 - [9] C. J. van Duijn, X. Cao, and I. S. Pop, *Two-phase flow in porous media: Dynamic capillarity and heterogeneous media*, Transport in Porous Media **109**, 333–357 (2015), analyzes two-phase flow with dynamic capillary effects in heterogeneous media, highlighting the transition between hyperbolic and regularised regimes.
 - [10] X. Cao, I. S. Pop, *et al.*, *Degenerate two-phase porous media flow model with dynamic capillarity*, Journal of Differential Equations **260**, 2418–2456 (2016), provides mathematical analysis of a degenerate elliptic–parabolic (pseudo-parabolic) two-phase flow model including dynamic capillary pressure, with existence/uniqueness results.
 - [11] C.-W. Shu, *High order weno and dg methods for time-dependent convection-dominated problems*, Journal of Computational Physics **316**, 598–658 (2016), survey of high-order finite volume/WENO and discontinuous Galerkin methods for hyperbolic conservation laws relevant to saturation transport.
 - [12] G.-S. Jiang and C.-W. Shu, *Weighted essentially non-oscillatory (weno) methods*, Journal of Computational Physics **126**, 202–228 (1996), foundational work on high-resolution WENO reconstruction for hyperbolic PDEs.
 - [13] N. Gerhard *et al.*, *Multiwavelet-based grid adaptation with discontinuous galerkin schemes*, Journal of Computational Physics **301**, 265–288 (2015), adaptive multiresolution strategies using multiwavelets integrated into DG frameworks for hyperbolic conservation laws.
 - [14] G. Kesserwani *et al.*, *(multi)wavelets increase both accuracy and efficiency of standard godunov-type hydrodynamic models*, Advances in Water Resources **144**, 103693 (2020), multiwavelet adaptivity combined with FV and DG solvers to enhance adaptivity and efficiency.
 - [15] O. P. L. Maître and O. M. Knio (Springer, 2017) Chap. 18, pp. 637–672.
 - [16] S. H. Fouladi, M. Hajiramezanali, H. Amindavar, J. A. Ritcey, and P. Arabshahi, *Denosing based on multivariate stochastic volatility modeling of multiwavelet coefficients*, IEEE Transactions on Signal Processing **61**, 5578–5589 (2013).
 - [17] J. Sembiring, A. S. Sabzevary, and K. Akizuki, *Stochastic process on multiwavelet*, IFAC Proceedings Volumes **35**, 211–215 (2002), 15th IFAC World Congress.
 - [18] A. Harten, *Adaptive multiresolution schemes for shock computations*, Journal of Computational Physics **115**, 319–338 (1994).
 - [19] N. Hovhannisyanyan, S. Müller, and R. Schäfer, *Adaptive multiresolution discontinuous galerkin schemes for conservation laws*, Mathematics of Computation **83**, 113–151 (2014).
 - [20] D. Caviedes-Voullième *et al.*, *Multiwavelet-based mesh adaptivity with discontinuous galerkin methods*, Applied Mathematical Modelling (2020), please verify full bibliographic metadata from your database before submission.
 - [21] N. Gerhard, *A wavelet-free approach for multiresolution-based grid adaptation for conservation laws*, Journal of Scientific Computing (2022), please verify full bibliographic metadata from your database before submission.
 - [22] J. Huang and Y. Cheng, *An adaptive multiresolution discontinuous galerkin method for scalar hyperbolic conservation laws in multidimensions*, SIAM Journal on Scientific Computing (2020), please verify volume, issue, pages, and DOI before submission.
 - [23] F. Male, *Pywaterflood: Well connectivity analysis through capacitance-resistance modeling*, Journal of Open Source Software **9**, 6191 (2024).
 - [24] G. Chavent and J. Jaffré, *Mathematical Models and Finite Elements for Reservoir Simulation: Single Phase, Multiphase and Multicomponent Flows through Porous Media*, Studies in Mathematics and its Applications, Vol. 17 (North-Holland, Amsterdam, 1986).
 - [25] B. Alpert, *A class of bases in l^2 for the sparse representation of integral operators*, SIAM Journal on Mathematical Analysis **24**, 246–262 (1993), <https://doi.org/10.1137/0524016>.
 - [26] B. Cockburn and C.-W. Shu, *Runge–kutta discontinuous galerkin methods for convection-dominated problems*, Journal of Scientific Computing **16**, 173–261 (2001).
 - [27] J. S. Hesthaven and T. Warburton, *Nodal Discontinuous Galerkin Methods: Algorithms, Analysis, and Applications* (Springer, New York, 2008).
 - [28] B. Cockburn and C.-W. Shu, *Tvb runge–kutta local projection discontinuous galerkin finite element method for conservation laws. iii. one-dimensional systems*, Journal of Computational Physics **84**, 90–113 (1989).
 - [29] V. V. Rusanov, *Calculation of interaction of non-steady shock waves with obstacles*, USSR Computational Mathematics and Mathematical Physics **1**, 304–320 (1961).
 - [30] S. K. Godunov, *A difference scheme for numerical solution of discontinuous solution of hydrodynamic equations*, Matematicheskii Sbornik **47**, 271–306 (1959).
 - [31] X. Zhang and C.-W. Shu, *On maximum-principle-satisfying high order schemes for scalar conservation laws*, Journal of Computational Physics **229**, 3091–3120 (2010).
 - [32] S. Gottlieb, C.-W. Shu, and E. Tadmor, *Strong stability-preserving high-order time discretization methods*, SIAM Review **43**, 89–112 (2001).
 - [33] R. Courant, K. Friedrichs, and H. Lewy, *On the partial difference equations of mathematical physics*, IBM Journal of Research and Development **11**, 215–234 (1967).